

Large-Scale Fading Behavior for a Multi-Cellular Network with Uniform Spatial Distribution

Mouhamed Abdulla* and Yousef R. Shayan

Department of Electrical and Computer Engineering, Concordia University, Montréal, Canada

E-mail: {m_abdull, yshayan} @ ece.concordia.ca

Abstract

Tractably characterizing the actual position of nodes for large wireless networks is technically unfeasible. Thus, stochastical spatial modeling is commonly considered for emulating the random pattern of mobile users. As a result, the concept of random geometry is gaining traction in cellular systems in order to analytically extract hidden features and properties useful for assessing the performance of networks. Meanwhile, the large-scale fading between interacting nodes is a fundamental element in radio communications, responsible for weakening the propagation, and thus worsening the service quality. Given the importance of channel losses in general, and the inevitability of random networks in real-life situations, it was then natural to merge these two paradigms together in order to obtain an improved stochastical model for the large-scale fading indicator. Therefore, in exact closed-form notation, we generically derived the large-scale fading distribution between a reference base-station and an arbitrary node for a multi-cellular random network model. In fact, we for the first time provided an explicit and definitive formulation that considered at once: the lattice profile, the users' random geometry, the effect of the far-field phenomenon, the path-loss behavior, and the stochastic impact of channel scatters. The veracity and accuracy of the theoretical analysis was also confirmed through Monte Carlo simulations.

Keywords—Cellular networks; large-scale fading; Monte Carlo simulations; random number generation; spatial distribution.

1. Introduction

1.1 – Objective

For wireless communications, large-scale fading (LSF) is indeed a fundamental factor for ensuring transmission between a base-station (BS) and a mobile-station (MS). In fact, due to its prerequisite for a host of network metrics including outage probability, the density function for the path-loss (PL) or the received power level have been previously shown for a fixed predetermined separation between an MS and a BS [1–5]. The aim in this paper is to reconsider this analytical problem for a multi-cellular network (MCN) architecture by generalizing the channel-loss distribution between any uniformly-based random positioned node and a reference BS. Evidently, this PDF can typically be obtained experimentally based on Monte Carlo (MC) simulations. However there are two leading reasons why this approach is inconvenient: 1) random simulation is an inefficient computationally expensive approach; 2) the obtained result is analytically intractable. These factors are further testaments for the necessity to obtain an explicit, generic and rigorous theoretical derivation for the LSF density.

1.2 – Related Work

In the recent years, some relevant work in this direction for the random uniform spatial distribution model has gradually emerged; this effort is chronicled as follows. Initially, the contribution of [6] found the PL density for uniformly deployed nodes in a fixed circular cell. Then, an attempt to simplify this density result through curve fitting was shown in [7]. Next, we generalized in [8] the above analysis in order to ensure spatial adaptability for various disk-based surface regions, along with multi-width rings and circular sectors. Furthermore, we derived in [9] the exact LSF distribution for a MCN between a random node and a reference BS located at the centroid of a hexagonal cell. Following the publication of our paper, using a slightly different approach, another paper appeared that also determined the PL density within a hexagonal cell and provided approximate options [10].

However, these outcomes did not specifically take into account a comprehensive and precise analysis that incorporated at once: the structure of the network configuration, users' nodal geometry, the effect of the far-field phenomenon, the PL predictive behavior, and the impact of channel shadowing due to in-field scatterers. Thus, while remaining generic and scalable for different network purposes, we aim here to accurately and explicitly solve this challenge by holistically formulating the propagation fundamentals of the LSF model for an adaptable random MCN pattern.

1.3 – Organization

The rest of this paper is organized as follows. In Section 2, we will set the stage for network analysis by jointly assimilating the fundamental characteristics of: spatial uniformity, lattice geometry, and radiation modeling. Then, in Section 3, the efficient and unbiased random network emulation geared for channel analysis will be developed. Afterward, in Section 4, the LSF distribution analysis will be derived, and the exact closed-form stochastic result will be verified using MC experimentations. Finally, Section 5 will close the paper.

2. Characteristics of the Network Model

2.1 – Uniform Spatial Distribution

Despite various conjectures for reconstructing a network, the random uniform distribution assumption has been considered in analytical research, e.g. [11–16]. Essentially, if we consider we consider $A_0 \in \mathbb{R}_+^*$ to be the surface area of a particular network lattice, and $n_0 \in \mathbb{N}^*$ to represent the scale of the architecture, then the uniform areal density will be given by $\rho_0 \triangleq n_0/A_0$. Generally, this simple spatial realization is feasible when no major information about the network site is available.

2.2 – Geometrical Alterations for Simplifying Channel Analysis

As shown in Figure 1, geometrical changes to the emulated network model can be applied in order to simplify the analysis. Indeed, it is clearly possible to dismember the hexagonal cell into smaller

repetitive forms. In fact, the equilateral triangle is the most elementary portion of this cell model. Thus, considering this sub-pattern for internodal analysis will alleviate the derivation complexity of the LSF distribution because the formulation only depends on the reference to mobile separation, and is unaffected by the sectors rotation angle. Moreover, for planar deployment, the areal density will not affect the channel analysis since that the network spatial distribution will remain *random* and *uniform*.

3. Random Network Modeling for Analysis

3.1 – Geometrical Analysis

The characteristics described by nodal homogeneity, lattice geometry, and far-field radiation phenomenon, must collectively be incorporated in the spatial properties of the random network. In principle, this integration has a dual purpose: 1) It will be used to stochastically model the random lattice and effectively derive the PL density function for the entire network between a reference and an arbitrary terminal; 2) It will be employed to emulate actual random pattern instances, and numerically verify by means of MC simulations the precision of the anticipated LSF formulation.

To proceed, in Figure 2 the hexagonal cell is represented with the far-field region. In this surface model, the cellular size $L \in \mathbb{R}_+^*$ and the far-field limit $r_0 \in \mathbb{R}_+^*$ are the essential elements that define the entire geometry of the network structure. For notational convenience, we will define a parameter for the cellular radius to the close-in distance ratio (RCR): $\mu \triangleq L/r_0$. From this model, we can determine the support range for the RCR indicator such that the layout of the lattice is accordingly preserved; namely: $\{r_0 < L/2\} \cap \{r_0 < \sqrt{3}L/2\} = \{\mu \in \mathbb{R}_+^* \mid \mu > 2\}$.

An expression in Cartesian coordinate notation for the spatial density function of a network cluster can be obtained via the deployment area, i.e.: $f_{XY}(x, y) = 1/A_{FF} = 12/(3\sqrt{3}L^2 - 2\pi r_0^2)$. As for the marginal PDF for the nodal geometry along the x -axis, it can be computed as follows:

$$f_X(x) = \int_{(x,y) \in D_{FF}} f_{XY}(x,y) dy = \left\{ 12 / (3\sqrt{3}L^2 - 2\pi r_0^2) \right\} \times \left\{ \left(\sqrt{3}x - \sqrt{r_0^2 - x^2} \right) \cdot \mathbf{1}(r_0/2 \leq x \leq r_0) + \sqrt{3}x \cdot \mathbf{1}(r_0 \leq x \leq L/2) + \sqrt{3}(L-x) \cdot \mathbf{1}(L/2 \leq x \leq L) \right\} \quad (1)$$

3.2 – Random Spatial Generation

The most efficient way to randomly generate arbitrary instances would be to consider the inverse transformation method (ITM), which is only possible through the use of the inverse CDF (ICDF). In other words: $\hat{x} = \{(F_X)^{-1}(\hat{u} \sim \mathcal{U}(0,1))\} \sim f_X(x)$, where $\mathcal{U}(0,1)$ is a standard uniform distribution [17]. Clearly, the precondition in this approach requires the availability of the ICDF in explicit notation, which is actually impossible to achieve for the marginal density of (1). As an alternative, the acceptance rejection method (ARM) can be used for random number generation (RNG) [18]. Granted, this iterative process is suboptimal when compared to the ITM technique; nonetheless, we will develop an approach for modifying the ARM algorithm in order to maximize its performance.

Consider the distribution function $f_X(x) : D_X \mapsto \mathbb{R}^+$, where the domain of the density is $D_X \triangleq [x_\alpha, x_\beta]$, and its associated extremities are given by $x_\alpha \triangleq \min_{\chi \in \mathbb{R}} \chi$ and $x_\beta \triangleq \max_{\chi \in \mathbb{R}} \chi$ such that $\chi \equiv \arg \{ \inf \{ f_X(x) > 0 \} \} \subset (x \in \mathbb{R})$. Then, based on the ARM procedure, we would need to determine some continuous arbitrary bonding function, say $\pi_b(x) : D_X \mapsto \mathbb{R}^+$, that covers the domain of $f_X(x)$, while $\pi_b(x) \geq f_X(x)$. Moreover, this bounding function is expected to be an augmented version to some valid comparison PDF $\delta_X(x) : D_X \mapsto \mathbb{R}^+$. In fact, the most generic and simplest way would be to consider the uniform case for the comparison density, namely: $\delta_X(x) = \mathcal{U}_x(x_\alpha, x_\beta)$. And thus, the bounding function can be realized by $\pi_b(x) = k \delta_X(x) \quad \exists k \in \mathbb{R}_+^* : k \geq 1$. Meanwhile, the likelihood for accepting

a randomly generated sample is specified by the area below $f_x(x)$. In contrast, the remaining sector between $\pi_b(x)$ and $f_x(x)$ constitutes the rejection region of generated samples. In order to maximize the acceptance rate (AR) of arbitrary samples, we could in essence minimize the rejection region. This could for instance be leveraged by adjusting the growth constant k to k_{\min} , such that $k > k_{\min} \geq 1$. To get this element, we need to identify the maximum value of the PDF:

$$f_x^{\max} \triangleq \max_{x \in \mathbb{R}} \{f_x(x)\} \in \mathbb{R}_+^* \text{. Then, we perform the following association: } \inf_{k \in \mathbb{R}_+^*} \{\pi_b(x)\} = f_x^{\max} \text{,}$$

and so we realize that: $k_{\min} = f_x^{\max} / \delta_x(x) = f_x^{\max} / \mathcal{U}_x(x_\alpha, x_\beta) = f_x^{\max} (x_\beta - x_\alpha)$. Next, a decision for the suitability of a sample for random generation based on the ARM algorithm depends on the $f_x(\hat{v})/\pi_b(\hat{v})$ ratio, where $\hat{v} \sim \delta_x(x)$. This expression can further be elaborated as follows:

$$\frac{f_x(\hat{v})}{\pi_b(\hat{v})} = \frac{f_x(\hat{v})}{k \delta_x(\hat{v})} < \frac{f_x(\hat{v})}{k_{\min} \delta_x(\hat{v})} = \frac{f_x(\hat{v})}{f_x^{\max} (x_\beta - x_\alpha) \mathcal{U}_x(x_\alpha, x_\beta)} = \frac{f_x(\hat{v})}{f_x^{\max}} \quad (2)$$

If we apply (2) to the marginal PDF of (1), we then get:

$$\frac{f_x(\hat{v})}{f_x^{\max}} = 2 \left\{ \left(\hat{v} - \sqrt{(r_0^2 - \hat{v}^2)/3} \right) / L \cdot \mathbf{1}(r_0/2 \leq \hat{v} \leq r_0) + \hat{v}/L \cdot \mathbf{1}(r_0 \leq \hat{v} \leq L/2) + (1 - \hat{v}/L) \cdot \mathbf{1}(L/2 \leq \hat{v} \leq L) \right\} \quad (3)$$

After taking the above analysis into account, we then obtain the RNG algorithm for $\hat{x} \sim f_x(x)$ in Figure 3 that ensures an efficient approach for generating n_s samples. In Figure 4, the PDF along the x -axis is shown for two different values of RCR obtained by means of analysis and via MC simulations for $n_s = 15,000$ valid samples and with a histogram of $n_B = 150$ bins.

3.3 – Measuring the Performance of Efficient Random Generation

In this part, we are interested to quantify the performance of the obtained efficient RNG. Thus, we want to determine an expression for the corresponding AR. Following the logic detailed above, the

event of accepting a sample is defined as a subset of the universal space $\Omega = \{A, R\}$. Consequently, the AR as a function of RCR can be determined by:

$$p_A = \Pr\{A \subset \Omega\} = \int_{x=-\infty}^{\infty} f_X(x) dx / \int_{x=-\infty}^{\infty} \pi_b(x) dx = 1 / \int_{x=-\infty}^{\infty} k \delta_X(x) dx = 1 / k_{\min} \int_{x=-\infty}^{\infty} \mathcal{U}_X(x_{\alpha}, x_{\beta}) dx = 1 / k_{\min} = 1 / f_X^{\max}(x_{\beta} - x_{\alpha}) = (L^2 - 2\pi r_0^2 / 3\sqrt{3}) / L(2L - r_0) = (\mu^2 - 2\pi / 3\sqrt{3}) / \mu(2\mu - 1) \quad \mu > 2 \quad (4)$$

At this point, the natural intrigue is to analytically obtain the optimum RCR value that maximizes $p_A = p_A(\mu)$, which can be obtained by $dp_A(\mu) / d\mu = 0$; therefore resulting in a unique feasible solution given by: $\mu_{opt} = \{4\pi + \sqrt{2\pi(8\pi - 3\sqrt{3})}\} / 3\sqrt{3} \approx 4.57$. Hence, the efficient random generation approach developed can further be improved when $\mu = \mu_{opt}$, which essentially ensures an AR of $p_A(\mu_{opt}) \approx 0.529$. Pursuing this further, it is also worthwhile to characterize the AR as the RCR progressively increases, which can be evaluated by: $\lim_{\mu \rightarrow \infty} p_A(\mu) = 1/2$. In fact, it can be shown that $p_A = 0.5$ is indeed a horizontal asymptote (HA) of the $p_A(\mu)$ function.

In (4) we theoretically derived an expression for the AR. Conversely, we may also define a MC estimator for the acceptance probability of samples numerically assessed by $\tilde{p}_A = n_s / n_T$ such that $n_s \in \mathbb{N}$ represents the number of accepted samples and $n_T \in \mathbb{N}^*$ is the total number of randomly generated instances for a particular simulation realization. Assuming that n_T is deterministic, then the number of accepted samples will be random with distribution: $N_s \sim \text{Binomial}(n_s, n_T, p_A)$; having mean and variance equal respectively to $m_{N_s} = n_T p_A$ and $\sigma_{N_s}^2 = n_T p_A (1 - p_A)$. Then the statistics of the AR estimator can be shown to equal:

$$m_{\tilde{p}_A} = m_{\tilde{p}_A}(\mu) = E[\tilde{p}_A] = E[N_s / n_T] = m_{N_s} / n_T = p_A = (\mu^2 - 2\pi / 3\sqrt{3}) / \mu(2\mu - 1) \quad (5)$$

$$\begin{aligned}
\sigma_{\tilde{p}_A}^2 &= \sigma_{\tilde{p}_A}^2(\mu, n_T) = E\left[\left(\tilde{p}_A - m_{\tilde{p}_A}\right)^2\right] = E\left[\left(N_S/n_T - m_{\tilde{p}_A}\right)^2\right] \\
&= \sigma_{N_S}^2/n_T^2 = p_A(1-p_A)/n_T = \left\{1 - \left(\mu - 4\pi/3\sqrt{3}\right)^2/\mu^2(2\mu-1)^2\right\}/4n_T
\end{aligned} \tag{6}$$

Therefore, from (5) we realize that the AR estimator is *unbiased*, and from (6) we note that it is *consistent* because $\lim_{n_T \rightarrow \infty} \sigma_{\tilde{p}_A}^2 = 0$; meaning that an increase in n_T will improve this estimator at the expense of running time complexity. Furthermore, it is desired to minimize the variance of the AR estimator in order to enhance its predictability. Indeed, through the optimization of $\partial \sigma_{\tilde{p}_A}^2(\mu, n_T)/\partial \mu = 0$ and the plot of Figure 5, we determine that $\mu_{\sigma_{\min}} = \mu_{opt}$ is a feasible stationary point, and also detect a HA at $\sigma_{\tilde{p}_A}^2(\infty, n_T) = 1/4n_T$. Overall, we remark that selecting that $\mu \approx 4.57$ has a dual statistical advantage: 1) it maximizes the AR for RNG; 2) it minimizes the AR estimator variance.

For further insight of the AR behavior, in Figure 6, we show the corresponding theoretical and experimental plots. In fact, during MC simulations, for each μ value, $n_s = 10,000$ accepted samples are sought to estimate the AR. Overall, this RNG approach is reasonably similar to a coin toss for all possible realization because the AR of the efficient algorithm in Figure 3 is confined to: $0.47 < p_A(\mu) < 0.53$ $\mu \in (2, \infty)$.

3.4 – Geometrical Deployment on the Euclidian Plane

Efficient deployment along the x -axis was developed in the previous subsections. In this part, we will extend the treatment by deriving the spatial emplacement along the y -axis in order to generate random coordinates on the Euclidian plane. To do this, we require the conditional PDF which we obtain by the use of (1) alongside the deployment support of Figure 2, which produces:

$$\begin{aligned}
f_{Y|X=\hat{x}}(y) &= f_{XY}(\hat{x}, y)/f_X(\hat{x}) = \mathcal{U}_Y\left(\sqrt{r_0^2 - \hat{x}^2}, \sqrt{3}\hat{x}\right) \cdot \mathbf{1}(r_0/2 \leq \hat{x} \leq r_0) \\
&\quad + \mathcal{U}_Y\left(0, \sqrt{3}\hat{x}\right) \cdot \mathbf{1}(r_0 \leq \hat{x} \leq L/2) + \mathcal{U}_Y\left(0, \sqrt{3}(L - \hat{x})\right) \cdot \mathbf{1}(L/2 \leq \hat{x} \leq L)
\end{aligned} \tag{7}$$

In essence, depending on a particular sampling range for \hat{x} , the related PDF is then considered in the expression of (7) for randomly emulating the y -component of an arbitrary node. On the whole, the deployment complexity for the optimum spatial random generation can be assessed by integrating the algorithm of Figure 3 and the result formulated in (7) together: $O(n_T) + O(n_S) \sim O(n_S)$. Namely, the deployment of n_S random terminals has a computational cost of $O(n_S)$ provided $\mu \gg 2$. At last, to geometrically demonstrate the analysis reported in this section, we simulated in Figure 7 the random deployment for different nodal scales and RCR values.

4. Large-Scale Fading Analysis

4.1 – Spatial Density Model in Polar Notation

The spatial behavior elaborated in the previous section was done as groundwork for: general network emulation, formulation of the LSF density, and to numerically verify the authenticity of the analysis. In this part, we are interested to move forward by describing the stochastic characteristics of the channel-loss between an arbitrary node and a reference located at the origin of the service area. Given the nature of this problem, analysis in polar notation is favored; thus the joint density changes to:

$$f_{r\theta}(r, \theta) = f_{XY}(x, y) \Big|_{\substack{x=r\cos\theta \\ y=r\sin\theta}} \cdot \left| \det \begin{pmatrix} \partial x / \partial r & \partial x / \partial \theta \\ \partial y / \partial r & \partial y / \partial \theta \end{pmatrix} \right| = 12 \cdot r / (3\sqrt{3}L^2 - 2\pi r_0^2) \quad (r, \theta) \in D_{FF}^P \subset \mathbb{R}_+^2 \tag{8}$$

Using the law of sines to the marked blue triangle shown in Figure 2, an expression for the coverage radius can be obtained by $r_0 \leq r \leq r(\theta) = \sqrt{3}L/2 \sin(2\pi/3 - \theta)$ over $0 \leq \theta \leq \pi/3$. And therefore, the associated polar-based domain D_{FF}^P can be formulated as follows:

$$D_{FF}^P = \left\{ \begin{array}{ll} (r, \theta) \in \mathbb{R}_+^2; & 0 \leq \theta \leq \pi/3 : r \in [r_0, \sqrt{3}L/2]; \\ (r_0, L) \in \mathbb{R}_{+,*}^2 : & 0 \leq \theta \leq \arcsin(\sqrt{3}L/2r) - \pi/3 : r \in [\sqrt{3}L/2, L]; \\ r_0 < L/2 & 2\pi/3 - \arcsin(\sqrt{3}L/2r) \leq \theta \leq \pi/3 : r \in [\sqrt{3}L/2, L] \end{array} \right\} \quad (9)$$

4.2 – Characterizing Radial Distribution

From (8) and (9), we could now derive the radial distribution:

$$f_R(r) = \int_{(r, \theta) \in D_{FF}^P} f_{R\theta}(r, \theta) d\theta = \left\{ 4\pi r / (3\sqrt{3}L^2 - 2\pi r_0^2) \right\} \cdot \mathbf{1}(r_0 \leq r \leq \sqrt{3}L/2) + \left\{ 8r \left\{ 3\arcsin(\sqrt{3}L/2r) - \pi \right\} / (3\sqrt{3}L^2 - 2\pi r_0^2) \right\} \cdot \mathbf{1}(\sqrt{3}L/2 \leq r \leq L) \quad (10)$$

This radial PDF can then be substantiated via MC experimentation. The simulation results are shown in Figure 8, where the theoretical plots for a unity cell are accordingly graphed over two RCR values. The outputs are also complemented through stochastic simulation of random samples. In principle, for a particular μ value, the spatial position of $n_s = 25,000$ random nodes is obtained in a manner similar to that carried in Figure 7. Then, the measure from the arbitrary node to the BS is simply computed by $\hat{r}_i = \sqrt{\hat{x}_i^2 + \hat{y}_i^2} : i = 1, 2, \dots, n_s$; and an $n_B = 250$ bin histogram is constructed and accordingly scaled for the purpose of a distribution plot.

4.3 – RNG Based on Radial Distribution

Having $f_R(r)$ leads us to appropriately remark that in order to verify the anticipated analytical formulation for LSF density, random MC data can also be generated straight from the radial distribution in addition to the Cartesian-based RNG analysis described in Section 3. To contrast the computational suitability of this generation option, we thus need to identify the RNG attributes of the radial PDF. It can in fact be shown that the most efficient ITM approach is unsuitable given that a closed-form ICDF is unattainable. As a workaround, the modified version of the ARM procedure can

be considered for enhancing the generation performance of the radial probability distribution. Following the notation derived in (4), the utmost AR for the modified iterative algorithm becomes:

$$p_A^{Radial}(\mu) = 1/f_R^{\max}(r_\beta - r_\alpha) = 1/\max_{r \in \mathbb{R}} \{f_R(r)\} \cdot (L - r_0) = 3(\mu^2 - 2\pi/3\sqrt{3})/2\pi\mu(\mu-1) \quad \mu > 2 \quad (11)$$

Additionally, we can find the intersection point for the AR among the Cartesian and radial notations which is located at: $\mu_I = (2\pi - 3)/2(\pi - 3) \approx 11.59$. For comparison purposes, in Figure 9, we graph the AR for both of these RNG approaches. As shown, the AR for the radial distribution is monotonically decreasing, whereas the Cartesian alternative is not monotonic at all. Moreover, the HA of (11), which equals to $\lim_{\mu \rightarrow \infty} p_A^{Radial}(\mu) = 3/2\pi \approx 0.48$, reveals that Cartesian-based RNG is more performant as the RCR extends beyond μ_I . Overall, the optimum generation approach can thus be improved by partitioning the RCR range such that the AR is maximized. This leads us to observe the following association for further improvement to efficient random generation:

$$\begin{aligned} 2 < \mu \leq \mu_I &\leftrightarrow \text{radial RNG} \\ \mu > \mu_I &\leftrightarrow \text{Cartesian RNG} \end{aligned} \quad (12)$$

4.4 – Distribution of the Average Path-Loss

In general, it is shown (say [1]) that the average PL for mobile cellular communications is modeled by

$$\overline{L_{PL}(r)} = \overline{L_{PL}(r_0)} \cdot (r/r_0)^{n_{PL}}, \text{ where } n_{PL} \in \mathbb{R}_+^* : n_{PL} > 1 \text{ is the PL exponent, and } r_0, r \in \mathbb{R}_{+,*}^2 : r_0 \leq r$$

denote respectively the close-in distance and the internodal gap. For analytical suitability, this expression may be mapped to simpler notations, where the average PL for an L sized cellular network at a generic internodal gap is characterized by $w(r) \equiv \overline{L_{PL}(r)}_{dB} = \alpha + \beta \log_{10}(r)$ over $0 < r_0 \leq r \leq L$. Also, its inverse, which will be required in the next step, equals to $r(w) = 10^{(w-\alpha)/\beta}$ where $w \in [w_0, w_L]$ are breakpoints interrelated to (10).

The objective now is to characterize the distribution of the average PL overlaying the randomness of nodal geometry; therefore, we perform the following stochastic transformation:

$$\begin{aligned}
w &= w(r \sim f_R(r)) \equiv \overline{L_{PL}(r)}_{dB} \sim f_w(w) = f_R(r = r(w)) / |dw(r)/dr|_{r=r(w)} \\
\therefore f_w(w) &= f_R\left(10^{(w-\alpha)/\beta}\right) / \left|\beta/\ln(10)r\right|_{r=10^{(w-\alpha)/\beta}} \\
&= \frac{\ln(10) \cdot 10^{(w-\alpha)/\beta}}{\beta} \left\{ \begin{array}{l} \frac{4\pi r}{(3\sqrt{3}L^2 - 2\pi r_0^2)} \cdot \mathbf{1}(r_0 \leq r \leq \sqrt{3}L/2) \\ + \frac{8r\{3\arcsin(\sqrt{3}L/2r) - \pi\}}{(3\sqrt{3}L^2 - 2\pi r_0^2)} \cdot \mathbf{1}(\sqrt{3}L/2 \leq r \leq L) \end{array} \right\}_{r=10^{(w-\alpha)/\beta}} \\
&= \frac{4 \cdot \ln(10) \cdot 10^{2(w-\alpha)/\beta}}{\beta(3\sqrt{3}L^2 - 2\pi r_0^2)} \left\{ \begin{array}{l} \pi \cdot \mathbf{1}(w_0 \leq w \leq w_I) - 2\pi \cdot \mathbf{1}(w_I \leq w \leq w_L) \\ + 6\arcsin\left(\sqrt{3}L/2 \cdot 10^{(w-\alpha)/\beta}\right) \cdot \mathbf{1}(w_I \leq w \leq w_L) \end{array} \right\}
\end{aligned} \tag{13}$$

4.5 – Large-Scale Fading Density with Shadowing

In this part, we will supplement the PDF for the average power loss by introducing the impact of shadowing. In fact, this critical component analytically characterizes the implication of scatterers in the propagation channel; thus, incorporating it in the PL model is of paramount importance. Basically, shadowing is accounted for by merely adding a random variable (RV) Ψ_{S-dB} to the average PL. It is imperative to note that the randomness of shadowing and the average PL are statistically uncorrelated. Therefore, the overall LSF distribution is obtained by convolving the corresponding density functions:

$$\begin{aligned}
L_{PL}(r)_{dB} &= \left\{ \overline{L_{PL}(r)}_{dB} + \Psi_{S-dB} \right\} \cdot \mathbf{1}(r_0 \leq r \leq L) \sim f_{L_{PL}}(l) = (f_w * f_\Psi)(l) \\
\therefore f_{L_{PL}}(l) &= \underbrace{\int_{\tau=-\infty}^{\infty} f_w(\tau) \cdot f_\Psi(l-\tau) d\tau}_{\text{path-loss}} \triangleq \underbrace{\int_{\tau=-\infty}^{\infty} f_0(\tau) d\tau}_{\text{shadowing}} \quad l \in \mathbb{R}
\end{aligned} \tag{14}$$

The shadowing entity is actually described by a zero-mean log-normal distribution with standard deviation (SD) σ_Ψ ; i.e.: $\Psi_{S-dB} \sim f_\Psi(\tau) = \mathcal{N}_s(0, \sigma_\Psi^2)$. And therefore, with some analysis, it can be demonstrated that $f_\Psi(l-\tau) = \mathcal{N}_s(l, \sigma_\Psi^2)$: $\tau \in \mathbb{R}$, $l \in \mathbb{R}_+^*$. As for the $f_w(\tau)$ part in (14), it is

obtained by the notation in (13) following an exchange of w by τ . Consequently, the integrand of (14) reduces to the expression in (15), and having a domain which is limited by:

$$\{\tau \in \mathbb{R}\} \cap \{0 < w_0 \leq \tau \leq w_L\} = \{\tau \in \mathbb{R}_+^* \mid w_0 \leq \tau \leq w_L\}.$$

$$\begin{aligned} f_0(\tau) &= f_w(\tau) \cdot \mathcal{N}_s(l, \sigma_\Psi^2) = \frac{2\sqrt{2} \ln(10) \cdot 10^{2(\tau-\alpha)/\beta}}{\sqrt{\pi} (3\sqrt{3}L^2 - 2\pi r_0^2) \beta \sigma_\Psi} \cdot \exp\left\{-(\tau-l)^2/2\sigma_\Psi^2\right\} \\ &\quad \times \left\{ \pi \cdot \mathbf{1}(w_0 \leq \tau \leq w_L) - 2\pi \cdot \mathbf{1}(w_L \leq \tau \leq w_L) + 6 \arcsin\left(\sqrt{3}L/2 \cdot 10^{(\tau-\alpha)/\beta}\right) \cdot \mathbf{1}(w_L \leq \tau \leq w_L) \right\} \\ &= \frac{2\sqrt{2} \ln(10) \cdot 10^{-2\alpha/\beta}}{\sqrt{\pi} (3\sqrt{3}L^2 - 2\pi r_0^2) \beta \sigma_\Psi} \cdot \exp\left\{\overbrace{2 \ln(10) \tau / \beta - (\tau-l)^2 / 2\sigma_\Psi^2}^{\triangleq q(\tau)}\right\} \\ &\quad \times \left\{ \pi \cdot \mathbf{1}(w_0 \leq \tau \leq w_L) - 2\pi \cdot \mathbf{1}(w_L \leq \tau \leq w_L) + 6 \arcsin\left(\sqrt{3}L/2 \cdot 10^{(\tau-\alpha)/\beta}\right) \cdot \mathbf{1}(w_L \leq \tau \leq w_L) \right\} \end{aligned} \quad (15)$$

Next, we could further arrange (15) by completing the square of the quadratic function $q(\tau)$ inside the exponential so that it becomes of the form: $q(\tau) = a(\tau - h)^2 + k$. After some arithmetical manipulations, we then recognize that: $a = -1/2\sigma_\Psi^2$, $h = \{l + 2\ln(10)\sigma_\Psi^2/\beta\}$, and $k = \{2 \cdot l \cdot \ln(10)/\beta + (\sqrt{2}\ln(10)\sigma_\Psi/\beta)^2\}$. Now, the exponential part of (15) can be reorganized:

$$\begin{aligned} \exp\{q(\tau)\} &= \exp\{a(\tau-h)^2 + k\} = \exp\{k\} \cdot \exp\{a(\tau-h)^2\} \\ &= \exp\left\{2 \cdot l \cdot \ln(10)/\beta + (\sqrt{2}\ln(10)\sigma_\Psi/\beta)^2\right\} \cdot \exp\left\{-(\tau - \{l + 2\ln(10)\sigma_\Psi^2/\beta\})^2 / 2\sigma_\Psi^2\right\} \\ &= 10^{2 \cdot l / \beta} \cdot \exp\left\{(\sqrt{2}\ln(10)\sigma_\Psi/\beta)^2\right\} \cdot \exp\left\{-(\tau - \{l + 2\ln(10)\sigma_\Psi^2/\beta\})^2 / 2\sigma_\Psi^2\right\} \end{aligned} \quad (16)$$

After substituting (16) into (15), we then find that:

$$\begin{aligned} f_0(\tau) &= \overbrace{\frac{2\sqrt{2} \ln(10) \cdot 10^{2(l-\alpha)/\beta}}{\sqrt{\pi} (3\sqrt{3}L^2 - 2\pi r_0^2) \beta \sigma_\Psi} \cdot \exp\left\{(\sqrt{2}\ln(10)\sigma_\Psi/\beta)^2\right\} \cdot \exp\left\{\frac{-1}{2\sigma_\Psi^2}(\tau - \{l + 2\ln(10)\sigma_\Psi^2/\beta\})^2\right\}}^{\triangleq K_0} \\ &\quad \times \left\{ \pi \cdot \mathbf{1}(w_0 \leq \tau \leq w_L) - 2\pi \cdot \mathbf{1}(w_L \leq \tau \leq w_L) + 6 \arcsin\left(\sqrt{3}L/2 \cdot 10^{(\tau-\alpha)/\beta}\right) \cdot \mathbf{1}(w_L \leq \tau \leq w_L) \right\} \end{aligned} \quad (17)$$

At present, the function in (17) is adequately ordered for the purpose of being integrated, where τ independent expressions are assigned to K_0 . Taken together, the LSF distribution of (14) can be split into three parts where each has a particular identifier:

$$f_{L_{PL}}(l) = \int_{\tau=-\infty}^{\infty} f_0(\tau) d\tau = K_0 \left\{ \underbrace{\int_{\tau=w_0}^{w_I} f_0^{(1)}(\tau) d\tau}_{\triangleq I_{LSF}^{(1)}(l)} + \underbrace{\int_{\tau=w_I}^{w_L} f_0^{(2)}(\tau) d\tau}_{\triangleq I_{LSF}^{(2)}(l)} + \underbrace{\int_{\tau=w_L}^{\infty} f_0^{(3)}(\tau) d\tau}_{\triangleq I_{LSF}^{(3)}(l)} \right\} \quad l \in \mathbb{R} \quad (18)$$

After pursuing the first integration, we obtain (19), where $z = z(\tau) = (\tau - \{l + 2 \ln(10) \sigma_{\Psi}^2 / \beta\}) / \sigma_{\Psi}$;

and $Q(z)$ is an alternate format of the complementary error function (ERFC).

$$\begin{aligned} I_{LSF}^{(1)}(l) &= \int_{\tau=w_0}^{w_I} f_0^{(1)}(\tau) d\tau = \pi \int_{\tau=w_0}^{w_I} \exp\left\{-\left(\tau - \{l + 2 \ln(10) \sigma_{\Psi}^2 / \beta\}\right)^2 / 2\sigma_{\Psi}^2\right\} d\tau \\ &= \pi \cdot \sigma_{\Psi} \int_{z=z_0}^{z_I} \exp(-z^2/2) dz = -\pi \sqrt{2\pi} \cdot \sigma_{\Psi} \cdot \{Q(z)\}_{z=z_0}^{z_I} \end{aligned} \quad (19)$$

The second integration of (18) is relatively similar to (19), and so it can readily be solved as follows:

$$I_{LSF}^{(2)}(l) = 2\pi \sqrt{2\pi} \cdot \sigma_{\Psi} \cdot \{Q(z)\}_{z=z_I}^{z_L} \quad (20)$$

At this point, we could get an intermediate result by adding (19) and (20) together:

$$I_{LSF}^{(1)}(l) + I_{LSF}^{(2)}(l) = \pi \sqrt{2\pi} \sigma_{\Psi} \left\{ 2\{Q(z)\}_{z=z_I}^{z_L} - \{Q(z)\}_{z=z_0}^{z_I} \right\} = \pi \sqrt{2\pi} \sigma_{\Psi} \{Q(z_0) - 3Q(z_I) + 2Q(z_L)\} \quad (21)$$

As for the third integration defined in (18), it is manifested by:

$$\begin{aligned} I_{LSF}^{(3)}(l) &= \int_{\tau=w_I}^{w_L} f_0^{(3)}(\tau) d\tau = 6 \int_{\tau=w_I}^{w_L} \exp\left\{-\left(\tau - \{l + 2 \ln(10) \sigma_{\Psi}^2 / \beta\}\right)^2 / 2\sigma_{\Psi}^2\right\} \cdot \arcsin\left(\frac{\sqrt{3}L}{2 \cdot 10^{(\tau-\alpha)/\beta}}\right) d\tau \\ &= 6 \cdot \sigma_{\Psi} \int_{z=z_I}^{z_L} \exp(-z^2/2) \cdot \arcsin\left(\sqrt{3}L \cdot 10^{-\sigma_{\Psi}z/\beta} / 2 \cdot 10^{\{\beta(l-\alpha)+2\ln(10)\sigma_{\Psi}^2\}/\beta^2}\right) dz \end{aligned} \quad (22)$$

If we combine the intermediate result of (21) and (22) together, we then get the notation in (23), where and $z = z(w(r))$ is a composed function of PL and geometrical separation as detailed by (24).

$$I_{LSF}(l) = \sigma_\Psi \left\{ \begin{aligned} & \pi\sqrt{2\pi} \cdot \{Q(z_0) - 3Q(z_I) + 2Q(z_L)\} \\ & + 6 \cdot \int_{z=z_I}^{z_L} \exp(-z^2/2) \cdot \arcsin\left(\sqrt{3}L \cdot 10^{-\sigma_\Psi z/\beta} / 2 \cdot 10^{\{\beta(l-\alpha) + 2\ln(10)\sigma_\Psi^2\}/\beta^2}\right) dz \end{aligned} \right\} \quad (23)$$

$$\begin{aligned} z_{0,I,L} &= z_{0,I,L}(l) = \left(\tilde{w} - \{l + 2\ln(10)\sigma_\Psi^2/\beta\} \right) / \sigma_\Psi \longleftrightarrow \tilde{w} = w_0, w_I, w_L \\ &= \left(\alpha + \beta \log_{10}(\tilde{r}) - \{l + 2\ln(10)\sigma_\Psi^2/\beta\} \right) / \sigma_\Psi \longleftrightarrow \tilde{r} = r_0, \sqrt{3}L/2, L \\ &= \left\{ \alpha - l + \ln\left(\tilde{r}^{\beta/\ln(10)} / 10^{2\sigma_\Psi^2/\beta}\right) \right\} / \sigma_\Psi \end{aligned} \quad (24)$$

As a reminder from (14), the l entry represents a random sample of the LSF between a reference and an arbitrary terminal. Due to the log-normal nature of shadowing, this variable is expected to be in \mathbb{R} ; yet from a practical standpoint, it is a.s. element in \mathbb{R}_+^* . For further precision, the range for this RV can additionally be narrowed-down. Indeed, the lower extremity of the LSF measure is analyzed in (25), where the optimization is split because the contributions from the average PL and shadowing are independent of each other. By the same token, the higher extremity for an L size cellular network model is obtained in (26).

$$l_0 \triangleq \min_{(r, \sigma_\Psi) \in \mathbb{R}_{+,*}^2} \{L_{PL}(r)_{dB}\} = \min_{r \in \mathbb{R}_+^*} \{\overline{L_{PL}(r)}_{dB}\} + \min_{\sigma_\Psi \in \mathbb{R}_+^*} \{\Psi_{S-dB} \sim \mathcal{N}_s(0, \sigma_\Psi^2)\} \approx \tilde{l}_0 = \alpha + \beta \log_{10}(r_0) - 3\sigma_\Psi \quad (25)$$

$$l_L \triangleq \max_{(r, \sigma_\Psi) \in \mathbb{R}_{+,*}^2} \{L_{PL}(r)_{dB}\} \approx \tilde{l}_L = \alpha + \beta \log_{10}(L) + 3\sigma_\Psi \quad (26)$$

In fact, these results respectively provide w.h.p. an approximation for the LSF extremities because within three SDs most randomly generated samples will be accounted for; i.e. with a confidence interval (CI) represented by: $\Pr\{|l - \overline{L_{PL}(r)}_{dB}| \leq 3\sigma_\Psi\} \approx 0.997300$. In Figure 10, we graphically demonstrate these observations where the average PL and the deviation from it caused by shadowing are accordingly depicted. Taken as a whole, we thus identify a tighter support range for l , given by:

$$\{l \in \mathbb{R}_+^* \mid 0 < \tilde{l}_0 \leq l \leq \tilde{l}_L < \infty\} \quad (27)$$

At this moment, we have all the necessary features to analytically assemble the PDF of the channel-loss. To be precise, from (18), we recognize that the density function is composed of two parts. The first part, which is designated by K_0 , is identified in (17). The second part, namely $I_{LSF}(l)$, is obtained in (23), and its associated variables were solved in (24). Next, the domain of the density function was detailed in (27), where the related boundaries were assessed in (25) and (26). Finally, the exact closed-form stochastic statement for the probability distribution of the LSF between a randomly positioned MS and a reference BS over a MCN model is explicitly shown in (28). Overall, the derived density result is generic due to the changeable parameters specified by the $\vec{\Lambda}$ array.

$$\begin{aligned}
f_{L_{PL}}(l, \vec{\Lambda}) = & \left\{ 4 \cdot \ln(10) \cdot 10^{2(l-\alpha)/\beta} / \beta (3\sqrt{3}L^2 - 2\pi r_0^2) \right\} \cdot \exp \left\{ \left(\sqrt{2} \cdot \ln(10) \sigma_\Psi / \beta \right)^2 \right\} \\
& \times \left\{ \begin{aligned} & \pi \cdot \{Q(z_0(l)) - 3 \cdot Q(z_l(l)) + 2 \cdot Q(z_L(l))\} \\ & + 3\sqrt{2/\pi} \cdot \int_{z=z_l(l)}^{z_L(l)} \exp(-z^2/2) \cdot \arcsin \left(\sqrt{3}L \cdot 10^{-\sigma_\Psi z / \beta} / 2 \cdot 10^{\{\beta(l-\alpha)+2\ln(10)\sigma_\Psi^2\}/\beta^2} \right) dz \end{aligned} \right\} \\
\bullet \vec{\Lambda} = & \{\alpha, \beta, \sigma_\Psi, r_0, L\} \in \mathbb{R}_{+,*}^5 \quad 0 < \tilde{l}_0 \lesssim l \lesssim \tilde{l}_L < \infty \\
\bullet Q(z) = & \operatorname{erfc}(z/\sqrt{2})/2 = \{1 - \operatorname{erf}(z/\sqrt{2})\}/2 \\
\bullet z_0(l) = & \left\{ \alpha - l + \ln \left(r_0^{\beta/\ln(10)} / 10^{2\sigma_\Psi^2/\beta} \right) \right\} / \sigma_\Psi \\
\bullet z_l(l) = & \left\{ \alpha - l + \ln \left((\sqrt{3}L/2)^{\beta/\ln(10)} / 10^{2\sigma_\Psi^2/\beta} \right) \right\} / \sigma_\Psi \\
\bullet z_L(l) = & \left\{ \alpha - l + \ln \left(L^{\beta/\ln(10)} / 10^{2\sigma_\Psi^2/\beta} \right) \right\} / \sigma_\Psi \\
\bullet \tilde{l}_0 = & \alpha + \beta \log_{10}(r_0) - 3\sigma_\Psi \\
\bullet \tilde{l}_L = & \alpha + \beta \log_{10}(L) + 3\sigma_\Psi \quad \blacksquare
\end{aligned} \tag{28}$$

4.6 – Experimental Validation by MC Simulations

Here, we will authenticate the expression for the LSF distribution of (28) by means of stochastic simulations. Generally speaking, the approach for the validation process is broken-down into three major steps: 1) For a given lattice structure and dimensions, the random network geometry of wireless

nodes is emulated via MC approach; 2) The LSF density for a particular channel environment is numerically estimated using the emulated spatial samples; 3) The analytically derived PDF is plotted and then compared with the stochastic estimation.

It is imperative to emphasize that the tractable expression of (28) is fully generic and thus can be adaptable for any cellular application and wireless technology, as long as user's spatial geometry is assumed to be random and uniform over a MCN grid. Although the obtained result is generic in nature, yet to examine its correctness, we will exclusively consider the channel parameters of IEEE 802.20 [19] for an urban macrocell as specified in Table I. The actual details for the MC simulations are outlined as follows:

- In Table I, the transmission radius L can take different values. We will however consider a cellular size of 600 m, which translates into an RCR of ~ 17.14 . Given this RCR value, we therefore realize from (12) that Cartesian-based RNG is more efficient.
- An $n_s = 10,000$ random samples for nodes 2D spatial position is required. In fact, the set of $\hat{x}_i : i = 1, 2, \dots, n_s$ random components are generated from the algorithm of Figure 3. After, based on these values, the \hat{y}_i counterparts are obtained using the approach described by (7).
- The distance \hat{r}_i between the reference BS and random nodes is then calculated using the simple Pythagorean theorem.
- After that, the average PL for each of the n_s random samples is computed by:

$$\hat{l}_i \triangleq \overline{L_{PL}(\hat{r}_i)}_{dB} = \alpha + \beta \log_{10}(\hat{r}_i) \quad i = 1, 2, \dots, n_s \quad (29)$$

- Next, values for shadowing are generated such that $\hat{n}_i \sim \mathcal{N}(0,1)$ are samples from a standard normal distribution in order to get instances of LSF as expressed by:

$$\hat{l}_i \triangleq L_{PL}(\hat{r}_i)_{dB} = \hat{l}_i + \hat{\psi}_i = \hat{l}_i + \sigma_{\psi} \hat{n}_i \quad i = 1, 2, \dots, n_s \quad (30)$$

- The uppermost plot of Figure 11 shows a scatter diagram for the LSF as a function of the BS-to-MS interpoint range. Specifically, each of the 10,000 instances is represented by a random point. For perspective to this MC realization, three deterministic plots, namely:

$\overline{L_{PL}(r)}_{dB}$, $\overline{L_{PL}(r)}_{dB} - 3\sigma_{\Psi}$, and $\overline{L_{PL}(r)}_{dB} + 3\sigma_{\Psi}$ over $r \in [r_0, L]$ are also shown so as to characterize the average PL and the ~99.7% CI of LSF caused by shadowing. Indeed, as noticeable from the figure, only a negligible of ~0.3% of samples can be found outside the delineation of the CI.

- Then, based on the described scatter plot, a histogram for the LSF measure is constructed. In this simulation, an $n_B = 100$ bin histogram is considered with equal width designated by $\Delta l_B \in \mathbb{R}_+^*$. Precisely, the bars of the histogram are positioned next to each other with no spacing among them. As for the quantity of occurrence per bar, they are accordingly scaled to reflect an estimate of the PDF; i.e. the occurrence is divided by the amount of random samples and the bin width. Once scaling is performed, we obtain the PDF estimation at discrete points, namely: $pdf_j : j = 1, 2, \dots, n_B$.

- Also, the CDF of the LSF measure for randomly positioned nodes is approximated by the following recursive relationship:

$$\begin{aligned} cdf_1 &= pdf_1 \cdot \Delta l_B \\ cdf_j &= cdf_{j-1} + pdf_j \cdot \Delta l_B \quad j = 2, 3, \dots, n_B \end{aligned} \tag{31}$$

- As shown in Figure 11, the PDF estimation is performed over two values of n_s . As expected, an increase of random samples produces a better estimate that appropriately matches the theoretically derived density function of the LSF.
- We remarked earlier in Table I that the cellular size varies from $L = 600 \rightarrow 3,500$ m.

Therefore, we find it intriguing to randomly simulate the LSF PDF as L changes. The result of this undertaking is shown in Figure 12. It is worth noting from the simulation that an increase in the cellular dimension raises the channel-loss interval, and as a result the first-moment of the PDF is further shifted to the right. Also, it is obvious that the analytical derivation of the PDF and the estimation are properly congruent to each other.

5. Conclusion

The main objective of this chapter was to describe the channel-loss density for a random LWN with respect to its service provider. In fact, such density can be obtained numerically using MC simulations. However this approach is computationally expensive, and also it does not produce a tractable and generic stochastic statement useful for analysis and interplay of input/output parameters. Consequently, in order to mathematically characterize with great precision the manifestation of the channel decay, we progressed into various technical steps.

In particular, we first had to explain the essential groundwork for the derivation of LSF density by specifying and combining the analytical features of the spatial homogeneity, the geometrical attributes of the MCN lattice, and the characteristics of radiation.

Next, we developed an efficient approach for emulating the geometry of the random MCN geared specifically for LSF analysis. This was done as a preliminary step in deriving the LSF distribution and also for verifying the authenticity of the derivation via actual spatial deployment. We also measured the performance of the RNG, and its stochastic features were theoretically formulated and experimentally evaluated.

Equipped with all the necessary steps, we then analytically derived the exact and closed-form expression for the LSF density function between a reference BS and a randomly positioned node. We then performed various MC simulations in order to ensure and confirm the veracity of the result. To be

precise, in this derivation we took into account a number of fundamentally important elements, namely: the cellular structure of the architecture, the nodal spatial emplacement, the far-field effect of the reference antenna, the PL behavior, and the impact of channel scatterers.

In fact, the final and overall stochastic expression of the LSF PDF expressed in (28), is entirely generic and can directly be adjusted to any cellular size L , close-in distance r_0 , PL parameters α and β , and shadowing features described by its SD σ_ψ . That is to say that the stochastic formulation was attained in such a way that it could be applied to numerous MCN applications and technologies having a particular scale, coverage, and channel features. In other words, as shown in Figure 13, the reported predictive result is adaptable via the insertion of related variables to the different network architectures, such as: femtocell, picocell, microcell, and macrocell systems.

Also, given the diversity of the transmission coverage for each of the listed network realizations, it is thus evident to recognize the variability of the RCR. Notably, for mobile applications that operate with microcell or macrocell networks, the RCR is generally in the order of ten or greater. As for femtocell and picocell communications, the RCR is typically smaller than this value. Therefore, when the RCR has a slighter level, the significance of the BS far-field radiation is more prominent. On the other hand, a superior RCR is marginally impacted by the far-field region. Nonetheless, this EM propagation phenomenon was explicitly considered in the derived density of the LSF model in order to characterize the laws of communications in a rigorous manner; and also to ensure the soundness of the stochastic expression for all type of cellular systems, irrespective of the network scheme.

Finally, as noted in Section 2, it is worthwhile to remark that the closed-form analytical expression of the compiled channel-loss PDF will still be applicative for all cellular network cases whether partitioned into three or six sectors, or left unpartitioned.

References

- [1] Rappaport TS. *Wireless Communications: Principles and Practice*. Prentice Hall PTR: New Jersey, 2002.
- [2] Goldsmith A. *Wireless Communications*. Cambridge University Press: New York, 2005.
- [3] Saunders SR. *Antennas and Propagation for Wireless Communication Systems*. John Wiley & Sons, 1999.
- [4] Seybold JS. *Introduction to RF Propagation*. Wiley: New Jersey, 2005.
- [5] Garg V. *Wireless Communications and Networking*. Morgan Kaufmann Publishers: California, 2007.
- [6] Bharucha Z, Haas H. The distribution of path losses for uniformly distributed nodes in a circle. *Research Letters in Communications* 2008.
- [7] Broyde Y, Messer H. “A cellular sector-to-users path loss distribution model,” In *Proc. of the 15th IEEE/SP Workshop on Statistical Signal Processing (SSP'09)*, 2009, pp. 321-324.
- [8] Abdulla M, Shayan YR, Baek JH. “Revisiting circular-based random node simulation,” In *Proc. of the 9th IEEE International Symposium on Communication and Information Technology (ISCIT'09)*, Incheon, South Korea, Sep. 2009, pp. 731-732.
- [9] Abdulla M, Shayan YR. “An exact path-loss density model for mobiles in a cellular system,” In *Proc. of the 7th ACM International Symposium on Mobility Management and Wireless Access (MobiWac'09), held in conjunction with MSWiM'09*, Tenerife, Canary Islands, Spain, Oct. 2009, pp. 118-122.
- [10] Baltzis KB. Analytical and closed-form expressions for the distribution of path loss in hexagonal cellular networks. *Wireless Personal Communications* 2011; 599-610.
- [11] Dong L, Petropulu AP, Poor HV. A cross-layer approach to collaborative beamforming for wireless ad hoc networks. *IEEE Trans. on Signal Processing* 2008; **56**(7): 2981-2993.
- [12] Omiyi P, Haas H, Auer G. Analysis of TDD cellular interference mitigation using busy-bursts. *IEEE Trans. on Wireless Communications* 2007; **6**(7): 2721-2731.
- [13] Mukherjee S, Avidor D, Hartman K. Connectivity, power, and energy in a multihop cellular-packet system. *IEEE Trans. on Vehicular Technology* 2007; **56**(2): 818-836.
- [14] Ochiai H, Mitran P, Poor HV, Tarokh V. Collaborative beamforming for distributed wireless ad hoc sensor networks. *IEEE Trans. on Signal Processing* 2005; **53**(11): 4110-4124.
- [15] Bettstetter C. On the connectivity of ad hoc networks. *Computer Journal* 2004; **47**(4): 432-447.
- [16] Abdulla M, Shayan YR. “Cellular-based statistical model for mobile dispersion,” In *Proc. of the 14th IEEE International Workshop on Computer-Aided Modeling, Analysis and Design of Communication Links and Networks (CAMAD'09)*, Pisa, Tuscany, Italy, Jun. 2009, pp. 1-5.
- [17] Abdulla M. On the Fundamentals of Stochastic Spatial Modeling and Analysis of Wireless Networks and its Impact to Channel Losses. Ph.D. Dissertation, Dept. of Electrical and Computer Engineering, Concordia Univ., Montréal, Québec, Canada, Sep. 2012.
- [18] Krishnan K. *Probability and Random Processes*. Wiley-Interscience: New Jersey, 2006.
- [19] IEEE 802.20 Channel Models Document. IEEE 802.20 PD-08r1.

Table I. MBWA channel model for urban macrocell.

IEEE 802.20 Propagation Parameters	
Propagation Model :	<i>COST-231 Hata-Model</i>
Operating Frequency :	1.9 GHz
Support Range :	$r_0 = 35 \text{ m} \leq r \leq L$ $600 \leq L \leq 3,500 \text{ m}$
Channel - Loss :	$\alpha = 34.5 \text{ dB}$ $\beta = 35 \text{ dB}$
Shadowing :	$\sigma_\psi = 10 \text{ dB}$

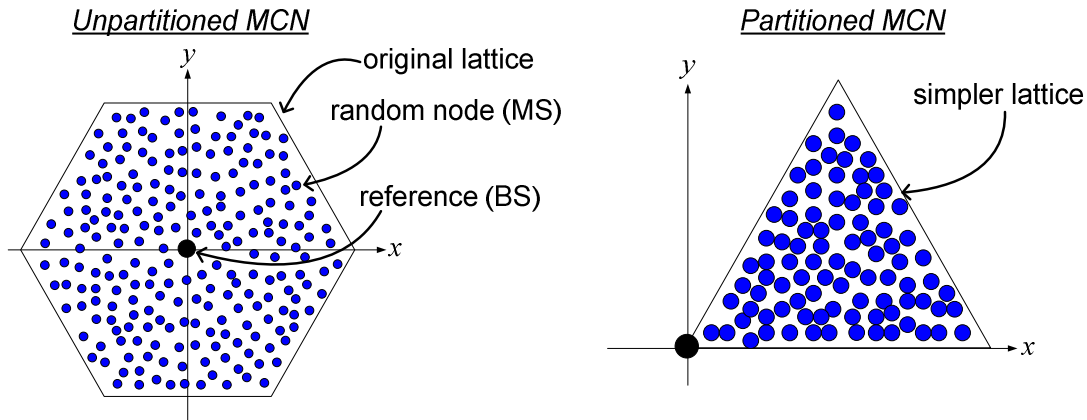


Figure 1. Simplifying BS-to-MS channel analysis via geometrical partitioning.

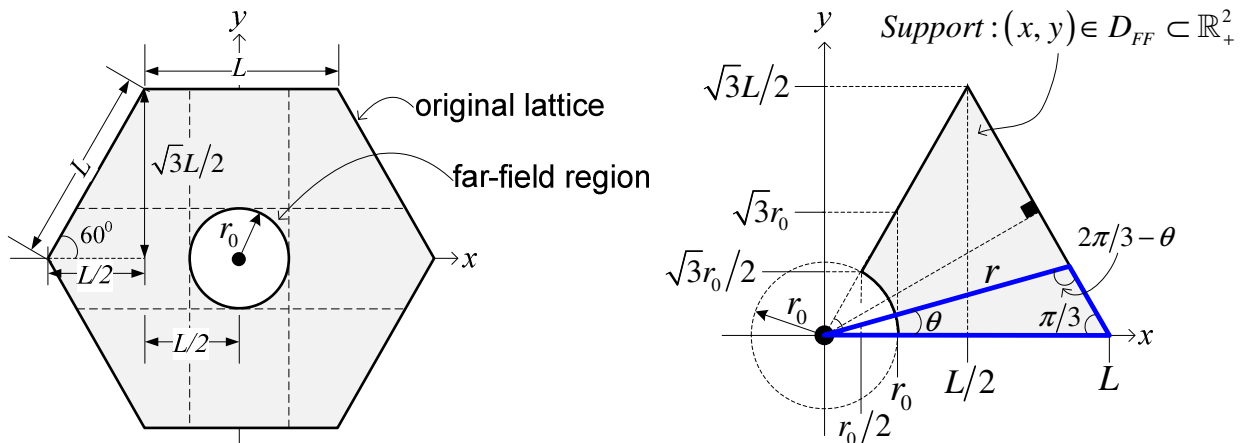


Figure 2. Dimensions of the random network deployment surface with far-field.

Algorithm 1 - Random Deployment with Far-Field Radiation along the x -axis

```

1:  Require:  $n_S \in \mathbb{N}^*$   $r_0 \in \mathbb{R}_+^*$   $L \in \mathbb{R}_+^*$ 
2:  Initialize:  $i = 0$   $n_T = 0$ 
3:  while  $\{i < n_S\}$  do
4:     $n_T := n_T + 1$ 
5:    Generate two i.i.d. RVs:  $\{\hat{u}_0, \hat{u}_1\} \sim \mathcal{U}(0,1)$ 
6:    Compute:  $\hat{v} = r_0/2 + \hat{u}_1(L - r_0/2) \sim \delta_x(x) = \mathcal{U}_x(r_0/2, L)$ 
7:    if  $\{r_0/2 \leq \hat{v} \leq r_0\}$  then
8:      if  $\{\hat{v} - \sqrt{(r_0^2 - \hat{v}^2)/3} > \hat{u}_0 L/2\}$  then
9:         $i := i + 1$ 
10:       Random sample is accepted:  $\hat{x}_i := \hat{v} \sim f_x(x)$ 
11:    end if
12:    else if  $\{r_0 \leq \hat{v} \leq L/2\}$  then
13:      if  $\{\hat{v} > \hat{u}_0 L/2\}$  then
14:         $i := i + 1$ 
15:        Random sample is accepted:  $\hat{x}_i := \hat{v} \sim f_x(x)$ 
16:      end if
17:    else if  $\{L/2 \leq \hat{v} \leq L\}$  then
18:      if  $\{\hat{v} < L(1 - \hat{u}_0/2)\}$  then
19:         $i := i + 1$ 
20:        Random sample is accepted:  $\hat{x}_i := \hat{v} \sim f_x(x)$ 
21:      end if
22:    end if
23:  end while
24:  Return/Compute:  $\{\hat{x}_i\}_{i=1,2,\dots,n_S}$   $\tilde{p}_A = n_S/n_T$ 


---



```

Figure 3. Pseudocode for efficient random generation.

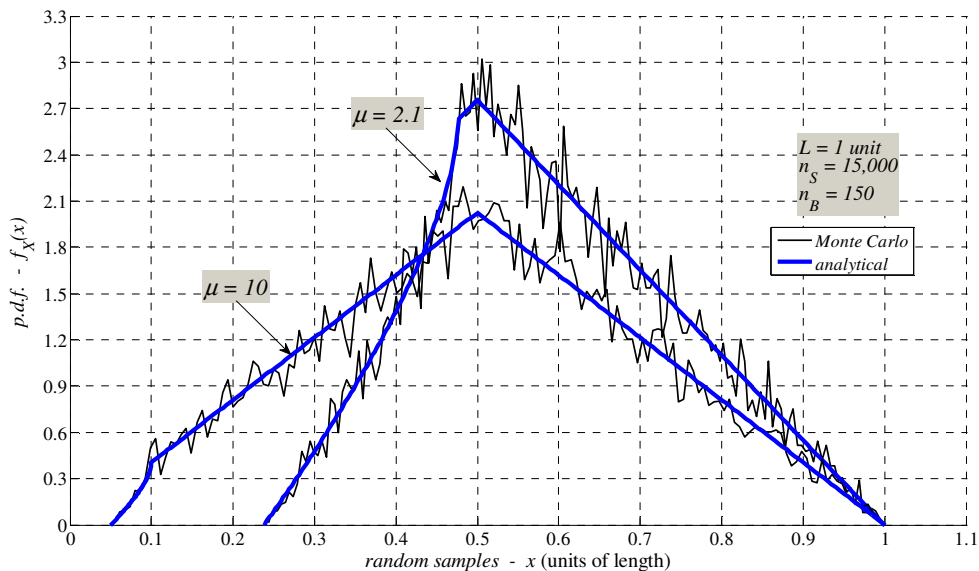


Figure 4. Marginal density of nodal geometry by means of random simulations.

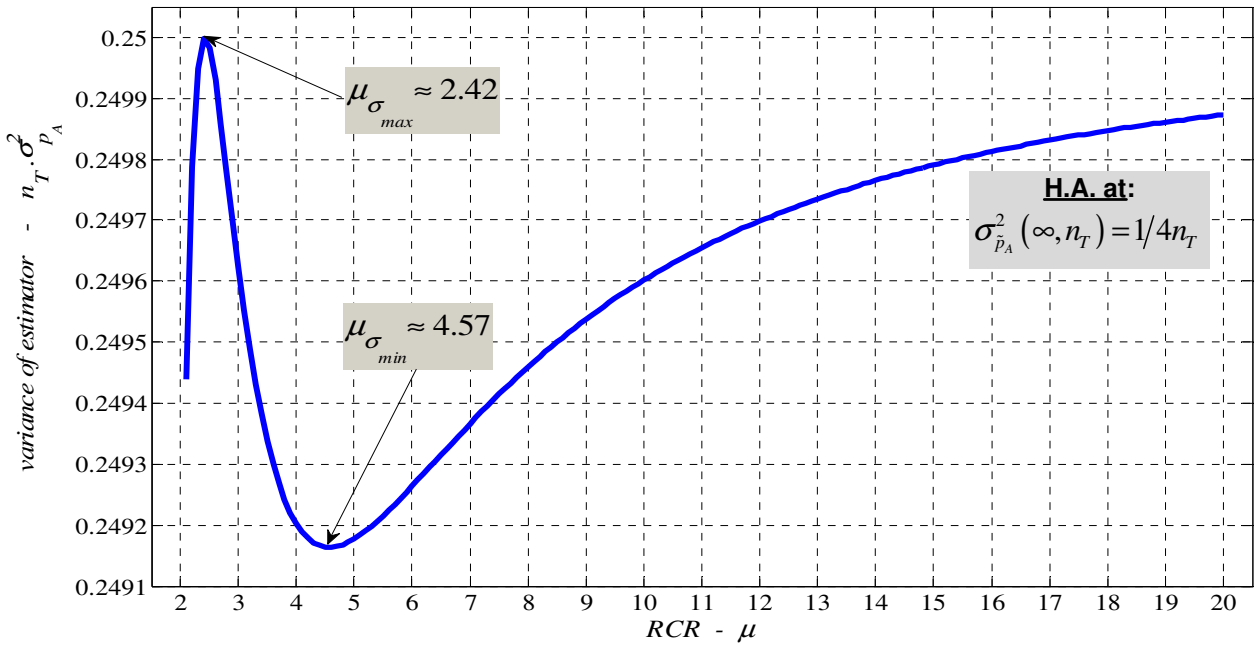


Figure 5. Impact of RCR on the AR estimator variance.

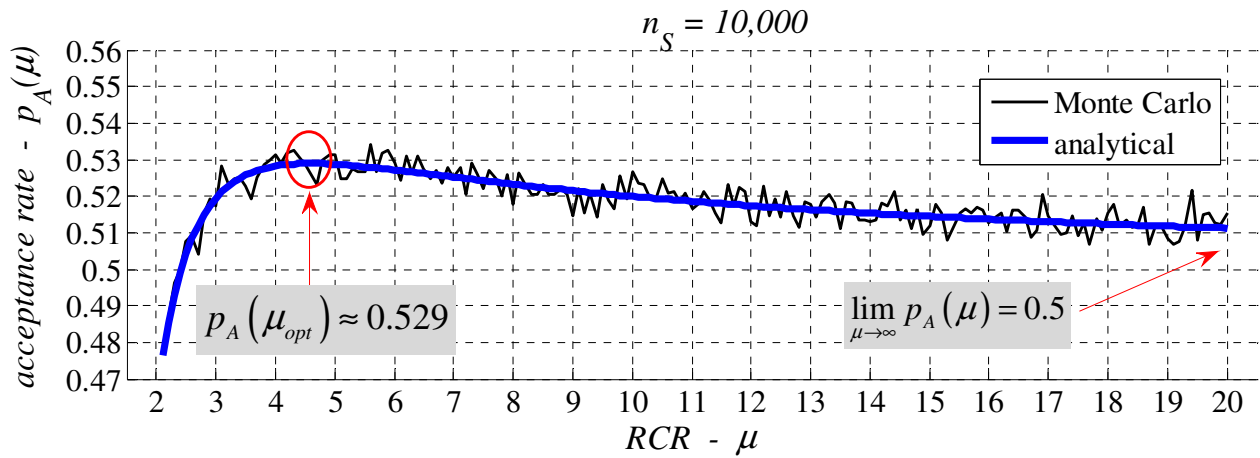


Figure 6. AR for efficient random generation versus RCR.

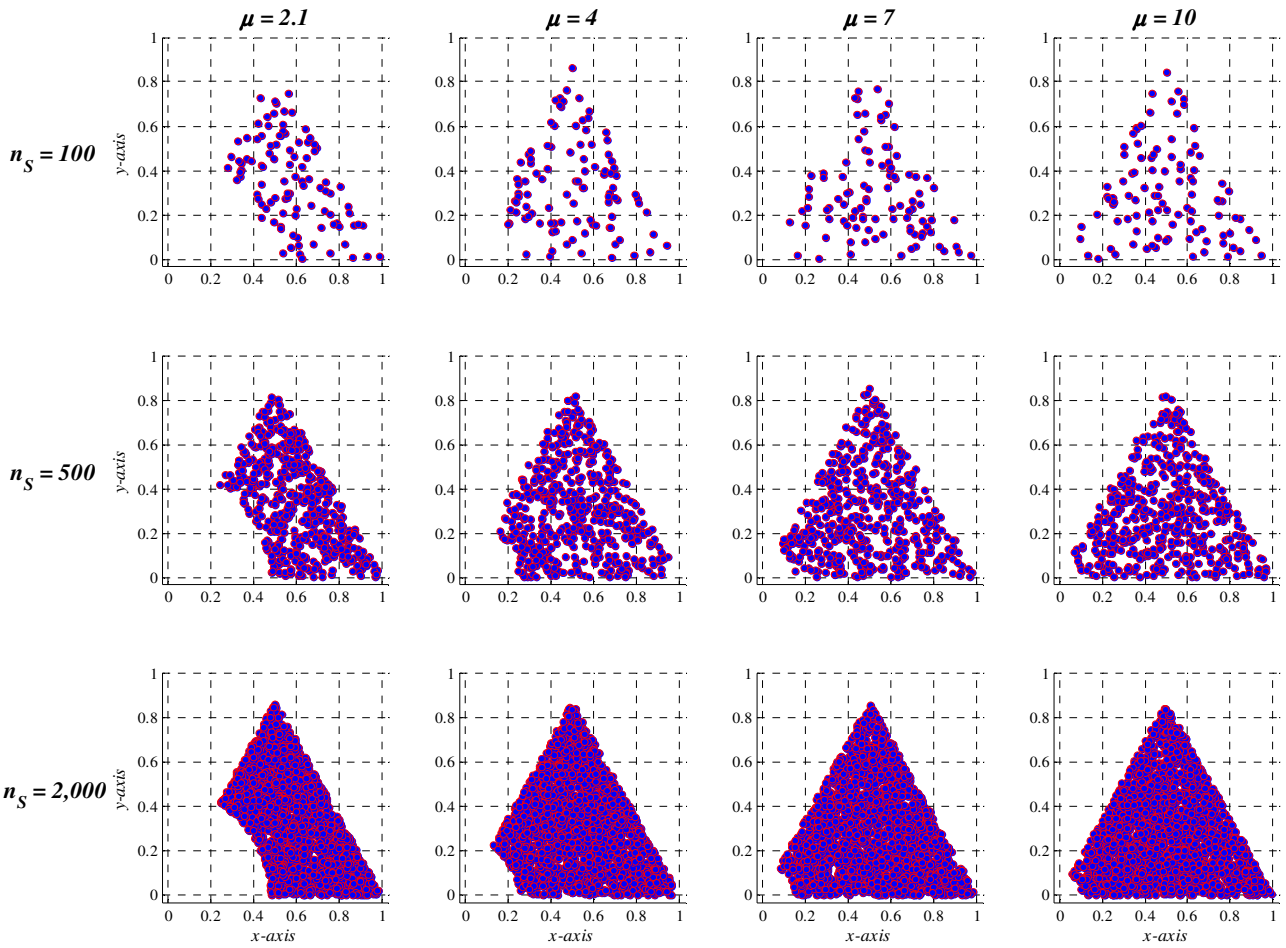


Figure 7. Random spatial emulation as a function of network scale and RCR values.

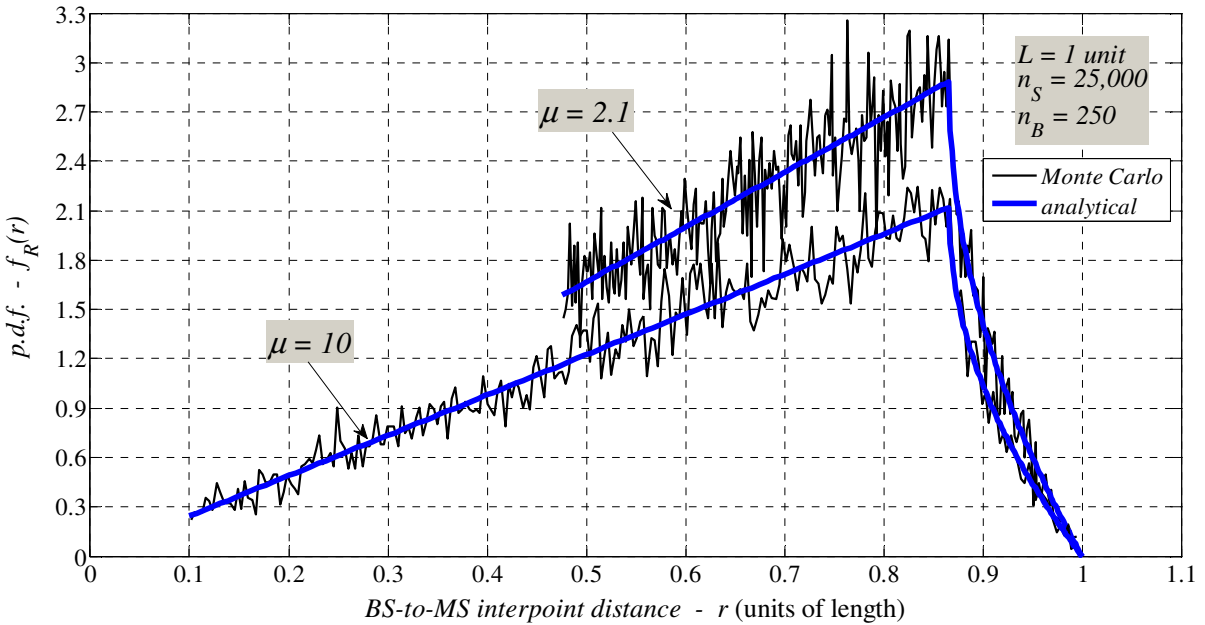


Figure 8. Radial distribution for nodal geometry via stochastic simulations.

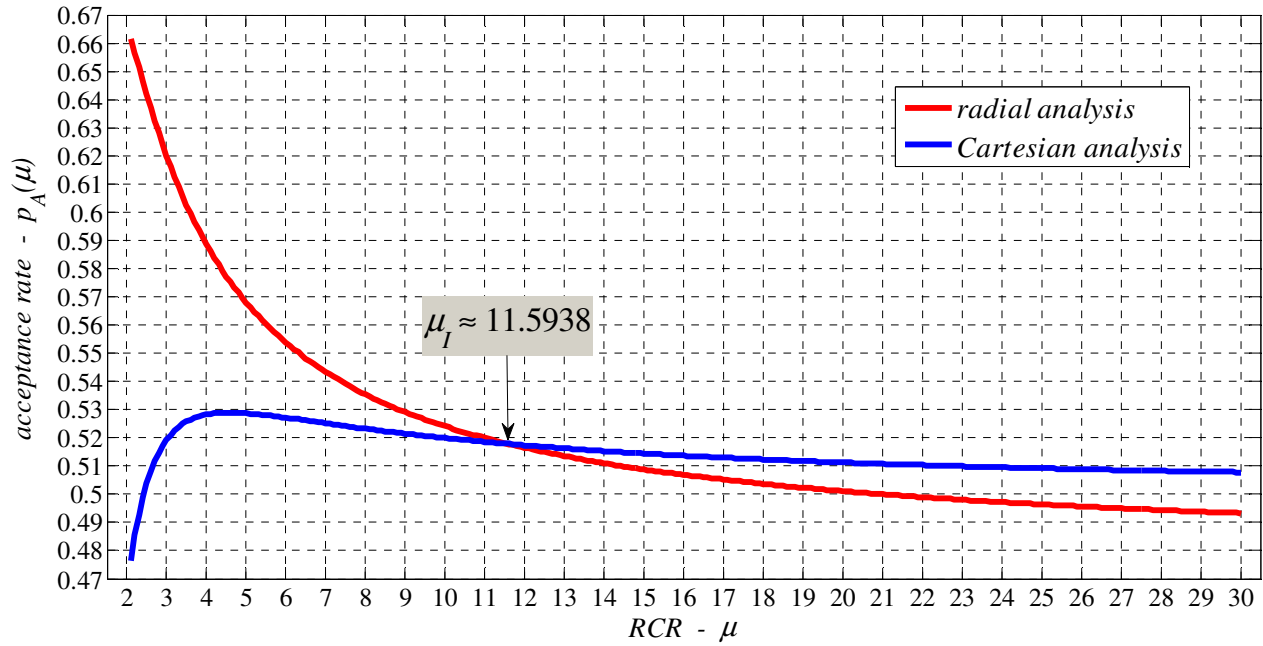


Figure 9. Efficient AR for RNG based on radial and Cartesian analysis.

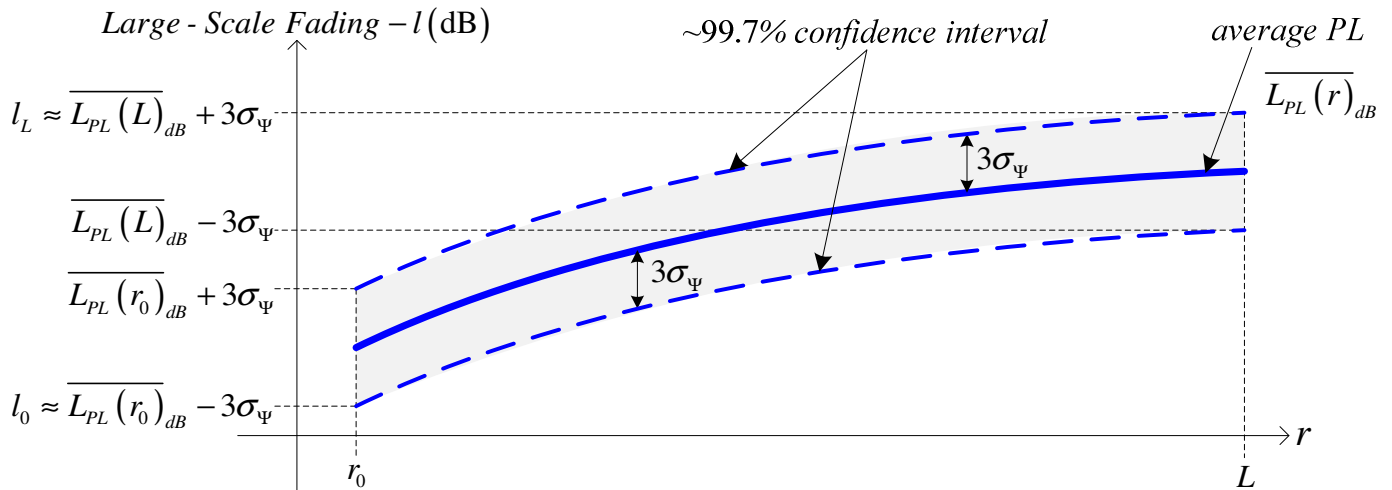


Figure 10. Interpreting the confidence interval and the extent of the LSF.

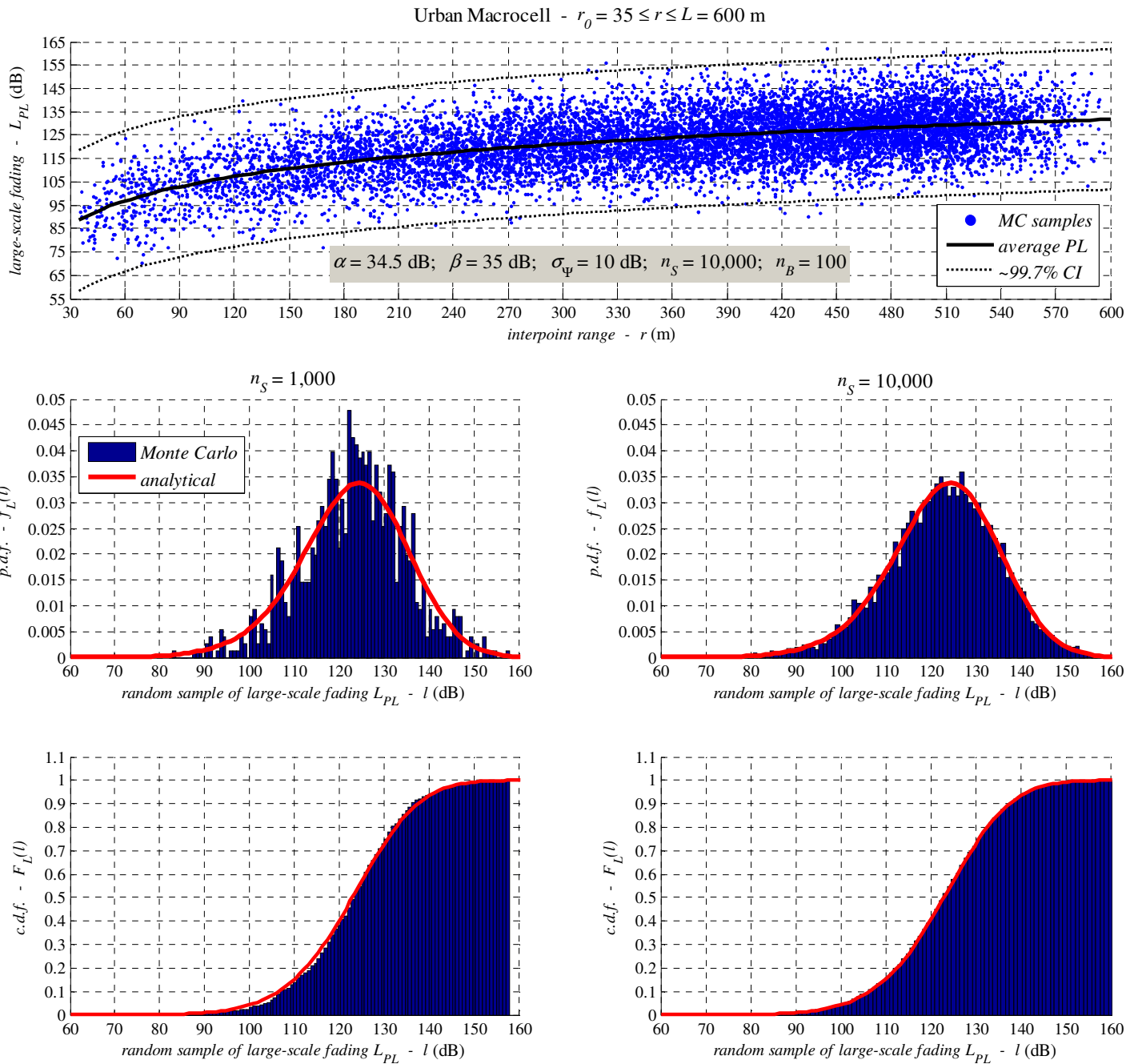


Figure 11. Verifying the analytically derived formulation for the LSF distribution.

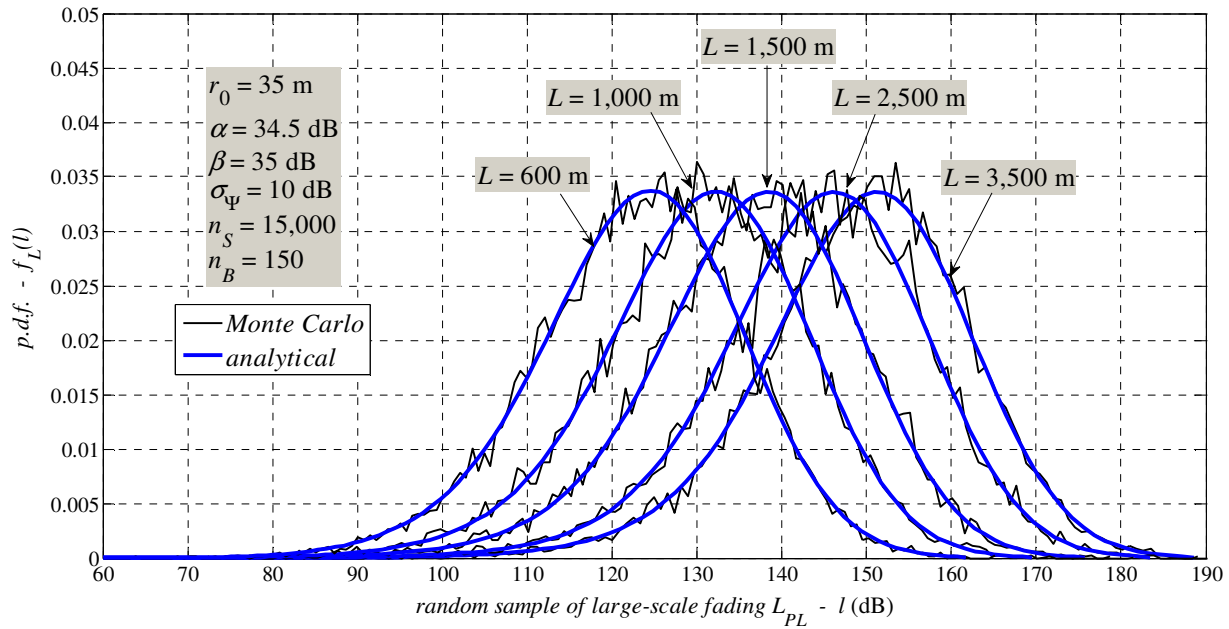


Figure 12. LSF distribution for BS-to-MS connections over different cellular sizes.

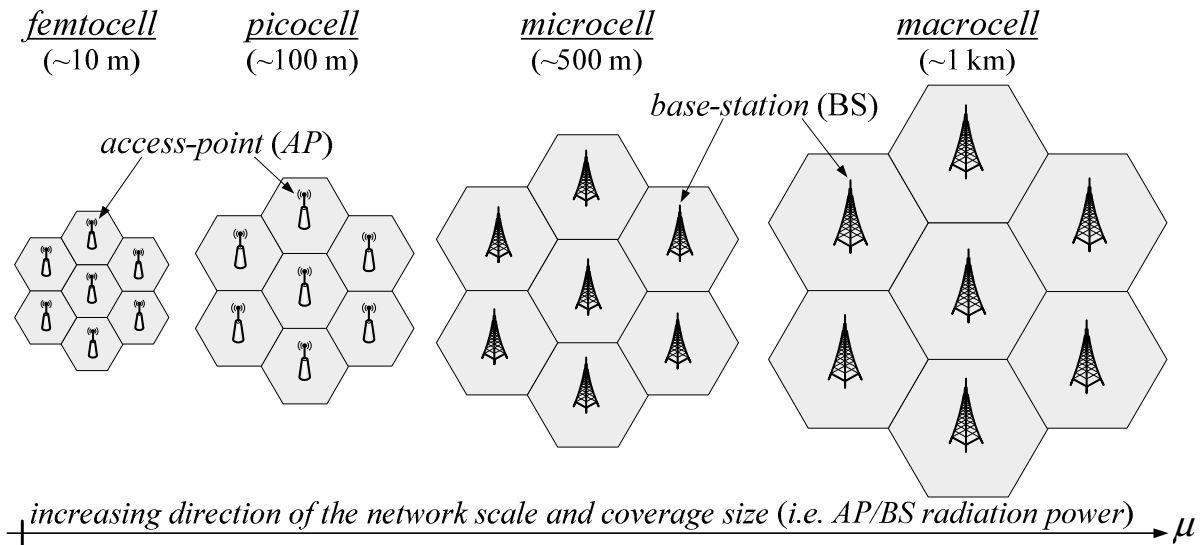


Figure 13. Feasibility of the MCN model for various deployment applications and purposes.



Mouhamed Abdulla is a Systems Engineering Researcher with the Department of Electrical and Computer Engineering at Concordia University in Montréal, Canada. He received, respectively in 2002, 2005, and 2012, a B.Eng. (with Distinction) in Electrical Engineering, an M.Eng. in Aerospace Engineering, and a Ph.D. in Telecommunications all at Concordia University. Moreover, for nearly 7 years since 2003, he worked at IBM Canada Ltd. as a Senior IT Specialist. Dr. Abdulla holds several awards and honors from academia, government, and industry; among them the Golden Key Outstanding Scholastic Achievement and Excellence Award (2009), and the IBM Innovation Award (2007). He is professionally affiliated with IEEE, IEEE ComSoc, IEEE GOLD, ACM, AIAA, and OIQ.

Currently, he is a member of the executive committee for IEEE Montréal Section, and serves as its Secretary. Furthermore, he is an Associate Editor of the *IEEE Technology News Publication*, *IEEE AURUM Newsletter*; and Editor of *Journal of Next Generation Information Technology*, and *Advances in Network and Communications Journal*. Also, he regularly serves as a referee for a number of journal publications such as: IEEE, Springer, and EURASIP; and contributes as an examination item writer for the prominent *IEEE/IEEE ComSoc WCET® Certification Program*. Presently, his research is focused on advancing the fundamentals and characteristics of wireless random networks. Moreover, he has a particular interest in philosophical factors related to engineering education, and research innovation. Since 2011, his biography was selected for inclusion in the distinguished Marquis Who's Who in the World publication.



Yousef R. Shayan received his Ph.D. degree in electrical engineering from Concordia University in 1990. Since 1988, he has worked in several wireless communication companies in different capacities. He has worked in research and development departments of SR Telecom, Spar Aerospace, Harris and BroadTel Communications, a company he co-founded. In 2001, Dr. Shayan joined the Department of Electrical and Computer engineering of Concordia University as associate professor. Since then he has been Graduate Program Director, Associate Chair and Department Chair. Dr. Shayan is founder of "Wireless Design Laboratory" at the department of Electrical and Computer Engineering which was established in 2006 based on a major CFI Grant. This lab has state-of-the art equipment which is used for development of wireless systems. In June 2008, Dr. Shayan was promoted to the rank of professor and was also recipient of "Teaching Excellence Award" for academic year 2007-2008 awarded by Faculty of Engineering and Computer Science. His fields of interests include wireless communications, error control coding and modulation techniques.